

Non-Unity Permeability in InP-Based Photonic Device Combined with Metamaterial

T. Amemiya¹, T. Shindo², S. Myoga², E. Murai²,
N. Nishiyama² and S. Arai^{1,2}

¹Quantum Nanoelectronics Research Center, Tokyo Institute of Technology,

²Dept. of Electrical and Electronic Engineering, Tokyo Institute of Technology,
Japan

1. Introduction

The relative permeability of every natural material is 1 at optical frequencies because the magnetization of natural materials does not follow the alternating magnetic field of light (see Fig. 1). If we can overcome this restriction and control both the permeability and the permittivity at optical frequencies, we will be able to establish a new field involving optical/photonic devices for future communication technologies. In this paper, we move one step closer to this goal—we demonstrate that in photonic devices, the relative permeability can be controlled by adopting metamaterials.

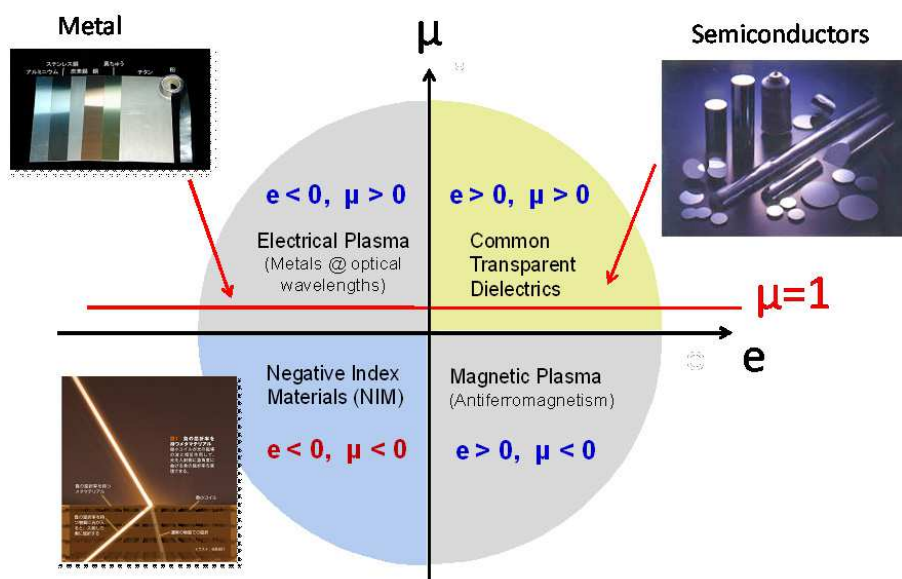


Fig. 1. Constitutive parameters at optical frequencies.

Metamaterials are artificial materials designed to have permittivity and permeability values that are not possible in nature [1]–[4]. They have recently attracted considerable interest because they exhibit unusual properties such as negative refractive indexes and have potential for unique applications such as high-resolution superlenses and invisibility cloaking devices [5, 6].

It is a challenging task to introduce the concept of metamaterials to actual photonic devices (see [7]–[12] for ordinary photonic devices). We hope to apply metamaterials to realize novel optical functionalities that can potentially establish a new field, *meta-photonics*. For this reason, many efforts have been expended in developing advanced optical applications using the concept of metamaterials. Some novel optical functionalities have been realized previously; for example, it has been shown that in theory, it is possible to achieve sophisticated manipulation of light such as slowing, trapping, and storing of light signals [13]–[18].

This paper provides an overview of the present state of research on novel photonic devices with the concept of metamaterials. In Section 2, we outline two promising approaches of making photonic devices combined with metamaterials. One of them is a fiber-based metamaterial device which functions nanoscale light source; another is a Si-based modulator which enables active tuning of metamaterials; the third has the form of III-V semiconductor-based waveguide combined with metamaterials which is compatible with other conventional photonic devices such as lasers and optical amplifier. Although these researches on *meta-photonics* are still in the experimental stage, they will probably reach a level of producing practical devices in the near future. In the succeeding sections, we focus on the III-V semiconductor-based waveguide combined with metamaterials shown in Fig. 2 and make a detailed explanation of the device. In Section 3, we take up the multimode-interferometer (MMI) as an example of photonic devices. First, theoretical investigations of the device are given. Actual devices based on this phenomenon are then developed.

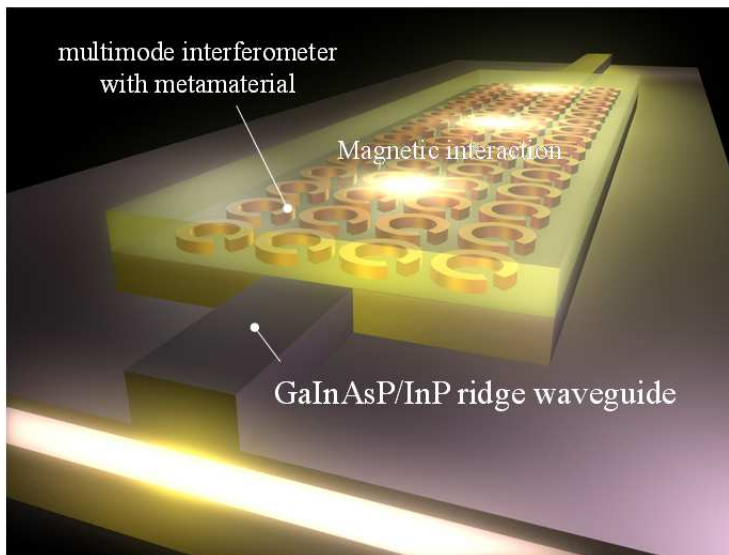


Fig. 2. III-V semiconductor-based waveguide optical device combined with metamaterials

The operating characteristics of the device, i.e., the transmission dependences on the polarization and wavelength of incident light, are also given in this Section. In Sections 4, we report a measurement method for retrieving accurate constitutive parameters (relative permittivity and permeability) from experimental data of the devices. We hope that this paper will be helpful to readers who are aiming to combine photonic integrated devices and metamaterials.

2. Recent progress in photonic devices using the concept metamaterials

2.1 Photonic devices combined with metamaterials

There are several strategies to develop advanced photonic applications which combine with metamaterial. The strategies can be classified into two types. One is based on the optical fiber as in conventional photonic communication system. Transferring the principle of metamaterials to a optical fiber system raises a number of inherent difficulties such as the decoherence of polarization rotation induced by structural birefringence. Therefore new idea is needed to use metamaterials in optical fiber structure. Sophisticated example is the nanoscale light sources consisting of fiber-coupled gold asymmetrically-split ring [19]. This device have attracted attention in recent years because of its compact techniques for producing the device. The other strategy is to combine semiconductor devices with metamaterials. Leading examples are the Si-based modulator which enables active tuning of metamaterial [20-22] and the III-V semiconductor-based waveguide in which relative permeability is not unity [23, 24]. The latter in particular is now the focus of attention because it is compatible with other standard waveguide-based optical devices such as lasers. In the following sections, we give the outline of the fiber-based nanoscale light sources and the Si-based modulator. The III-V semiconductor-based waveguide combined with metamaterials, which has been developed in our laboratory, is explained in detail in Section 3.

2.2 Fiber-based metamaterial device which functions nanoscale light source

Figure 3 shows a schematic of the fiber-based photonic metamaterial devices which act as nanoscale light sources. The device consists of fiber-coupled gold asymmetrically-split ring (ASR) array excited by an electron beam with a trajectory parallel to the surface. Light emission from nanoscale planar photonic metamaterials is induced by beams of free electrons, at wavelengths determined by both the dimensions of metamaterials and the electron beam energy. The ASR resonators are manufactured by focused ion-beam milling through ~70 nm gold films evaporated onto the end faces of standard or tapered optical fibers. Experiments are performed in a scanning electron microscope, which provided simultaneously for imaging and targeted electron beam excitation of samples.

In this device, energy is coupled from incident electrons to the plasmonic modes of the metamaterial structure for which propagating light modes then constitute a decay channel. Low energy beams of free-electrons can act as a broadband excitation sources for the collective plasmonic modes of photonic metamaterials, thereby driving resonant light emission at wavelengths determined by the structural design parameters of the metamaterial, which may be adjusted for operation across the visible to infrared range.

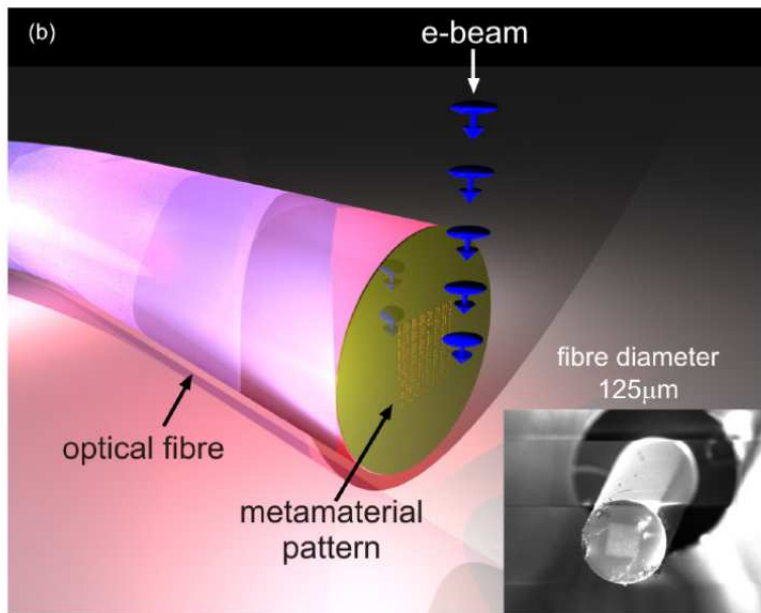


Fig. 3. Fiber-based photonic metamaterial devices which act as nanoscale light sources [19].

2.3 Si-based modulator which enables active tuning of metamaterials

When applying the concept of metamaterials to actual applications, it is indispensable to control properties of metamaterials for tuning electromagnetic responses (i.e., tunable metamaterials). A typical way to create tunable metamaterials is to integrate a reconfigurable material into a metamaterial structure; thereby the active tuning is achieved by applying an external stimulus. GaAs-based modulators with split ring resonators (SRRs) [25] and metamaterial memories on a VO₂ film [26] are such device prototypes operating at 1-10 THz.

Recent researches have shown that one can modulate the optical properties of a metamaterial on a sub-picosecond timescale enabling ultrafast photonic devices [20-22]. In these demonstrations, the authors used a fishnet structure metamaterial [27, 28] with two negative index resonances corresponding to two different periodic wavevectors of the internal gap-mode surface plasmon polaritons. Figure 4 shows one leading example of such device. The device reported here is composed of a BK7 glass substrate and a single metal-dielectric-metal (Ag/α-Si/Ag) functional layer with an inter-penetrating two-dimensional square array of elliptical apertures. In this device, the metamaterial is photoexcited with a visible pump pulse and then the pump-induced, time-resolved change in transmission ($\Delta T/T$) is measured around both the resonances. The longer wavelength resonance has a significantly stronger nonlinear response ($\Delta T/T \sim 70\%$) corresponding to its larger absolute value of the negative index and the stronger Drude response of photocarriers at longer wavelengths. These results provide insight into engineering various aspects of the nonlinear response of fishnet structure metamaterials.

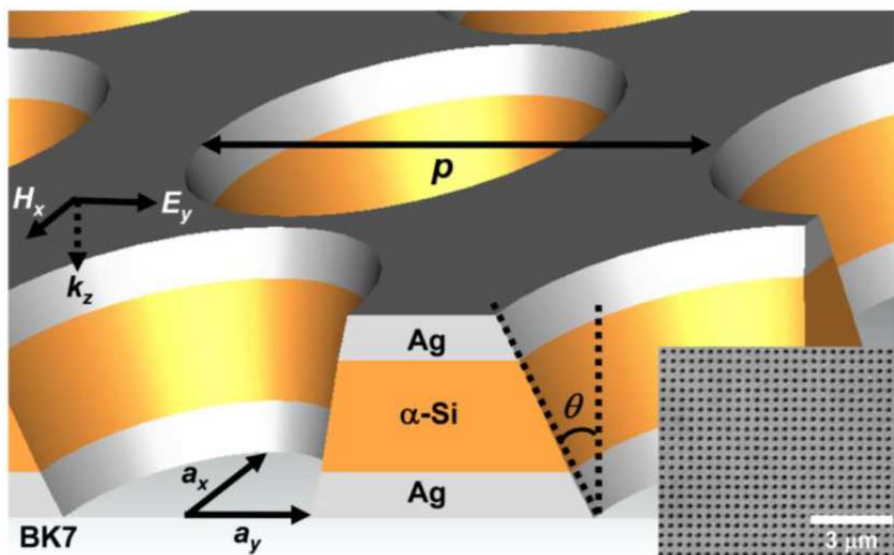


Fig. 4. Si-based modulator which enables active tuning of metamaterials [22].

3. III-V semiconductor-based waveguide optical device with metamaterials

3.1 Waveguide-based photonic devices combined with metamaterials

Encouraged by the results stated in Section 2, we consider introducing metamaterials into conventional photonic devices such as lasers, optical amplifiers, and modulators which have the form of III-V semiconductor-based waveguide. In this Section, the feasibility of employing semiconductor-based photonic devices combined with split-ring resonator (SRR)-based metamaterials is examined both theoretically and experimentally. We used a MMI as the stage of interaction between SRRs and light because the input light dispersed over the whole MMI and therefore gives no saturation to each SRR even if the light was very strong. First, theoretical investigations of the device structures of the SRRs and a MMI for use in the 1.5- μm -wavelength region are given in the former of this Section. Fabrication processes and operating characteristics of the device are then explained in the latter of this Section.

Our metamaterial MMI device is shown in Fig. 5. It consists of a waveguide-based GaInAsP/InP 1×1 MMI on which a gold SRR array is attached. If transverse electric (TE)-mode input light for the MMI has a frequency close to the SRR-resonant frequency, magnetic interactions occur between the TE light and SRR array. Therefore, the real part of the macroscopic permeability becomes large positive and negative at frequencies below and above SRR resonance, respectively. Consequently, the SRR array operates as a metamaterial layer to control permeability. The imaginary part of the permeability is not 0 but a finite value under this condition (this causes the absorption loss of light).

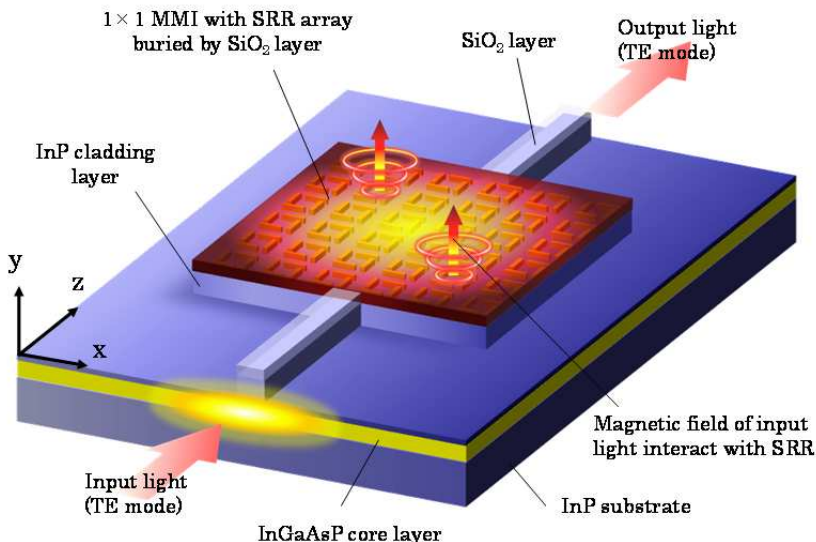


Fig. 5. InP-based 1×1 MMI with on which a gold SRR array is attached.

3.2 Theory of waveguide optical devices combined with metamaterials

The key is to create optical metamaterials that can be used to control permeability and obtain *non-unity* values at optical frequencies (note that, on the other hand, permittivity can be controlled more easily than permeability). A promising method for controlling permeability involves the use of a split-ring resonator (SRR). An SRR produces a circular current in response to an incident magnetic flux, thereby producing its own flux to enhance or oppose the incident field. Consequently, an array of extremely small SRRs operates as a metamaterial layer with non-unity permeability [29-33]. We now investigate the optimal structure of a four-cut SRR device for use at an optical frequency of 193 THz (corresponding to 1.55 μm wavelength for low-loss optical fiber communications). The transmission characteristics are obtained by considering the magnetic interactions between the SRRs and light traveling in the MMI.

A. Design of SRR structure for optical frequency

We must first determine the optimal dimensions of the SRR for the 1.5- μm -band frequency. Because the magnetic response of an SRR strongly depends on the conduction characteristics of the metal that forms the SRR, the dispersion of the internal impedance Z of the gold used in our SRRs was calculated. The internal impedance is the ratio of the surface electric field to the total current [34, 35]. Z for a unit length and unit width of a metal plane conductor is given by

$$Z(\tau) = \left(\sigma(\omega) \int_0^{\tau} \frac{\exp[ik(\omega)z] + \exp[ik(\omega)(\tau-z)]}{1 + \exp[ik(\omega)z]} dz \right)^{-1} \quad (1)$$

Here, $k(\omega)$ is given by

$$k(\omega) = \omega \sqrt{\epsilon_0 \mu_0} \left[1 + i \frac{\sigma(\omega)}{\omega \epsilon_0} \right], \quad (2)$$

where ω is the angular frequency of light, ϵ_0 and μ_0 are the permittivity and permeability of vacuum, respectively, τ is the thickness of the plane conductor, and $\sigma(\omega)$ is the conductivity of the metal as defined by the Drude model.

Figure 6 shows the internal impedance as a function of frequency for a gold layer whose thickness is larger than the penetration depth. As the frequency increases, the real part of the internal impedance first increases sharply and then saturates at around 100 THz; at frequencies higher than 100 THz, it gradually decreases. This dispersion property corresponds to the dielectric behavior of gold. In contrast, the imaginary part changes monotonously with frequency and has large negative values at optical frequencies; this corresponds to ohmic losses in gold.

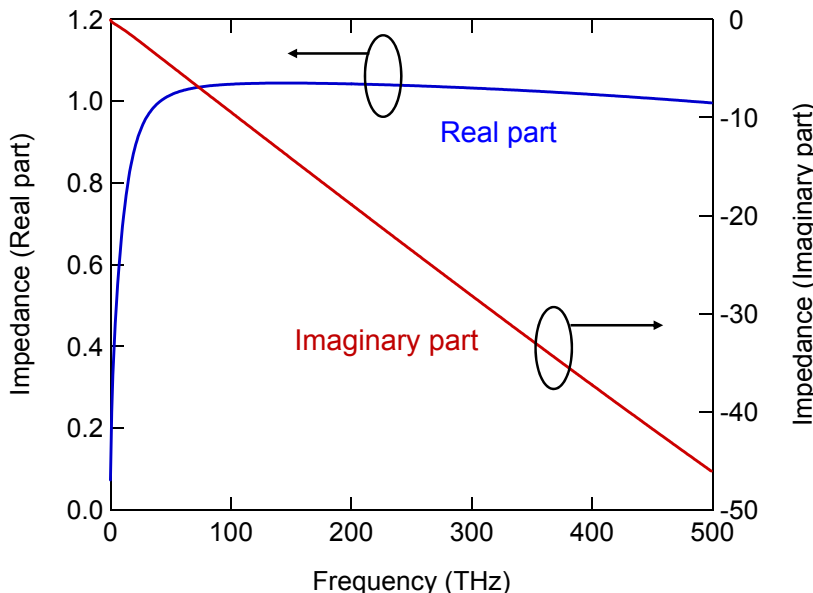


Fig. 6. Internal impedance of gold as a function of frequency (real part is surface resistivity, and imaginary part is internal reactance).

Using these dispersion curves, we calculated the magnetic response of a gold SRR at optical frequencies. A four-cut SRR was considered because it has high resonant frequency due to its small gap capacitance [36, 37]. The SRR was placed in a homogeneous host material (air), as shown in Fig. 5. If an incident AC magnetic field is applied to the SRR, an induced circular current flows in the ring through the gap capacitance. The circular current produces an internal magnetic field, and this produces a magnetic interaction between the SRR and light.

The total electromotive force (emf) induced around the SRR is given by the magnetic flux density B . Therefore, we can equate the potential drop to the emf as follows:

$$\begin{aligned} \partial_t \int_{SRR} Bd\sigma &= i\omega\mu_0 \int_{SRR} \left(H_{ext} + \frac{1}{4\pi} \oint \frac{jds \times r}{r^3} \right) d\sigma \\ &= V_{ring} + 4V_{gap} = \left[Z(\tau) \cdot \frac{4L}{W_1} - \frac{4W_2}{i\omega\epsilon_0\epsilon_m W_1 \tau} \right] j \end{aligned} \quad (3)$$

Here, we have used Biot-Savart's law. In this equation, H_{ext} is the magnetic field of light, ϵ_m and $Z(\tau)$ are the relative permittivity and internal impedance of gold, respectively, τ is the thickness of the SRR, j is the induced circular current in the SRR; and L , W_1 , and W_2 are the dimensions of the SRR (see Fig. 7(a)). The distribution of the magnetic field around the SRR can be calculated using Eq. 3, as illustrated in Fig. 7(b).

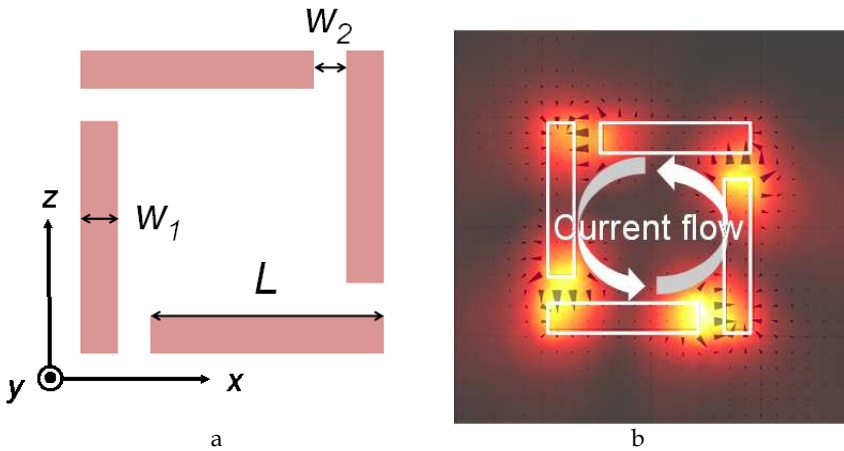


Fig. 7. Four-cut single SRR placed in glass: (a) plane pattern and (b) magnetic field distribution around the SRR at resonant frequency ($L = 300$ nm). The distribution of field intensity is visualized by a rainbow color map.

B. Macroscopic permeability of SRR array

The results for a single SRR were used to calculate the effective permeability of an SRR array taking into consideration a two-dimensional array layer comprising cubic unit cells, each with an SRR at its center; both the side lengths of each cell and the array pitch of the cells were d . For simplicity, the SRRs were assumed to be placed in air. The macroscopic permeability μ_{yy} of the SRR array layer can be calculated using the field averaging equation [38], and it is given by

$$\bar{\mu}_{yy} = \frac{\bar{B}_y(0, d/2, 0)}{\bar{H}_y(0, d/2, 0)} = \mu_0 \frac{(d)^{-2} \int_{-d/2}^{d/2} dx \int_{-d/2}^{d/2} H_z(x, d/2, z) dz}{(d)^{-1} \int_0^d H_z(0, y, 0) dy}, \quad (4)$$

where B_y and H_y with over lines represent the average values of magnetic flux density and magnetic field, respectively, in the SRR array layer. To get high accuracy in this homogenization approximation, the size of the integration region should be larger than the wavelength of light. In our calculation, we therefore integrated magnetic field over a large cubic region that contained a 3×3 cell array (this means that we replaced d with $3d$ in Eq. 4). Figure 8 shows the real and imaginary parts of permeability as a function of frequency, and the SRR size L is a parameter; here, W_1 and W_2 were set as 100 nm and d was 1.8 μm . The thickness τ of the SRR was set at twice the penetration depth of gold at each frequency. As L decreases, the magnetic resonant frequency increases. Magnetic response could be obtained at the 1.55- μm -band frequency (approximately 193 THz) for the SRR size L of 750 nm (red curves). As L decreases, the magnetic response becomes weaker because the inductance of each SRR decreases; this increases the effective resistance (or decreases the Q factor) of the SRR.

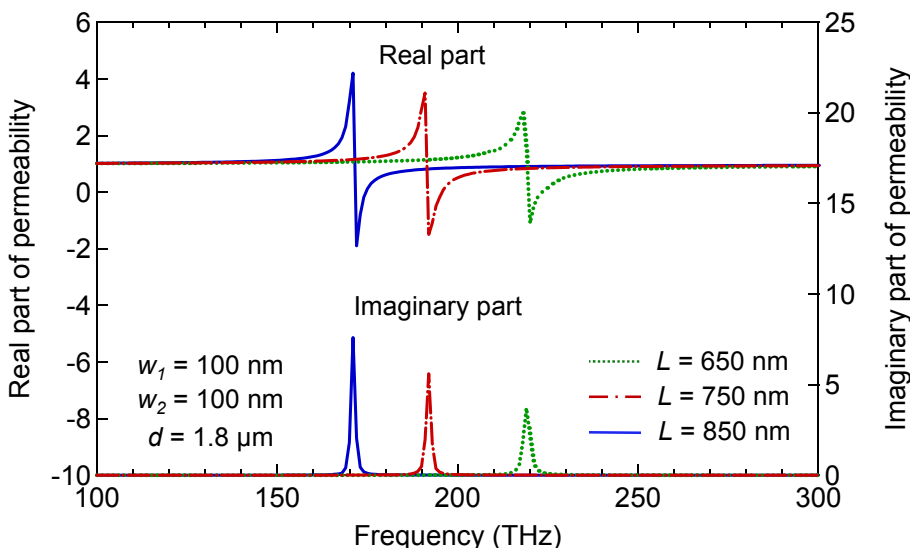


Fig. 8. Real and imaginary parts of the effective permeability of gold SRR array in air ($\epsilon = 1$) as a function of SRR size; here, $W_1 = W_2 = 100 \text{ nm}$, $d = 1.8 \mu\text{m}$, and frequencies = 100–300 THz.

Further, the magnetic response of the SRR array layer depends on the array pitch d . If d is large, the response is weak because the area density of SRRs is small; on the other hand, if d is small, the magnetic field in each SRR is canceled by the fields of the neighboring SRRs, and this weakens the total response of the SRR array layer.

C. Transmission characteristics of waveguide device with metamaterial

Using the abovementioned results, the transmission characteristics of an MMI with a metamaterial, which is shown in Fig. 5, were estimated using computer simulations based on the transfer-matrix method.

We first designed a device for use at 1.55- μm wavelength. The resultant structure is as follows. The substrate is an InP (refractive index $n = 3.16$). The constituent layers of the MMI are (i) a core guiding layer: 200-nm-thick $\text{Ga}_{0.25}\text{In}_{0.75}\text{As}_{0.54}\text{P}_{0.46}$ (bandgap wavelength $\lambda_g = 1.25 \mu\text{m}$; $n = 3.38$), (ii) InP upper cladding layer ($n = 3.16$), and (iii) SRR metamaterial layer: 50-nm-thick gold SRR array ($L = 750 \text{ nm}$; $W_1 = W_2 = 100 \text{ nm}$; $d = 1.6 \mu\text{m}$).

The thickness of the InP cladding layer affects the strength of interaction between the light traveling in the MMI and the SRR array attached to the surface of the cladding layer. Therefore, we determined the optimal thickness of the cladding layer from the following calculations.

After having designed the device structure, we calculated the transmission characteristics of the device as follows. The permeability tensor of the p -th layer, i.e., the InP substrate ($p = 1$), GaInAsP core layer ($p = 2$), InP upper cladding layer ($p = 3$), SRR array layer ($p = 4$), and air ($p = 5$), is given by

$$\tilde{\mu}_p = \begin{pmatrix} \mu_{xx}^p & 0 & 0 \\ 0 & \mu_{yy}^p & 0 \\ 0 & 0 & \mu_{zz}^p \end{pmatrix}, \quad (5)$$

where the diagonal elements μ_{xx} , μ_{yy} , and μ_{zz} are 1 at optical frequencies except in the SRR array layer. Using this tensor and the permittivity tensor ε_p for the p -th layer, Maxwell's equations are written as follows:

$$\begin{aligned} \nabla \times \mathbf{H} &= j\omega\epsilon_0\tilde{\varepsilon}_p\mathbf{E} \\ \nabla \times \mathbf{E} &= -j\omega\mu_0\tilde{\mu}_p\mathbf{H} \end{aligned} \quad (6)$$

We solved Eq. 6 under the condition that the electric and magnetic fields are invariant in the x -direction, that is, $\partial_x = 0$, and their tangential components are continuous at the boundary between the layers. For TE-mode light, the electric field E_x parallel to the z -axis is given by the following differential equation:

$$\partial_y^2 E_x + \left(k_0^2 \varepsilon_x \mu_z - \frac{\mu_z}{\mu_y} \beta^2 \right) E_x = 0 \quad (7)$$

where ε_x is the diagonal element of the permittivity tensor, and $k_0 = \omega\sqrt{\mu_0\varepsilon_0} = 2\pi/\lambda$ is the free-space propagation constant. The magnetic field H_z parallel to the z -axis (propagation direction) can be calculated using E_x as follows:

$$H_z = -\frac{j}{\omega\mu_0\mu_z} \partial_y E_x \quad (8)$$

An eigenvalue equation can be obtained using the boundary conditions with continuous E_x and H_z . In the calculations, we assumed that E_x and H_z decrease exponentially outside the GaInAsP guiding layer (i.e., in the air and the InP layers). For simplicity, we also assumed that all the layers except the SRR array layer are birefringent. The eigenvalue equation is given by

$$-\frac{j\beta_5}{\omega\mu_0\mu_z} \left(m_{11} - m_{12} \frac{j\beta_1}{\omega\mu_0\mu_z} \right) + \left(m_{21} - m_{22} \frac{j\beta_1}{\omega\mu_0\mu_z} \right) = 0, \quad (9)$$

where $m_{11}-m_{22}$ are given by

$$\begin{pmatrix} m_{11} & m_{12} \\ m_{21} & m_{22} \end{pmatrix} = \prod_{\text{All}} \begin{pmatrix} \cosh(\beta_n d_p) & \frac{j\omega\mu_0\mu_z}{\beta_n} \sinh(\beta_n d_p) \\ \frac{\beta_n}{j\omega\mu_0\mu_z} \sinh(\beta_n d_p) & \cosh(\beta_n d_p) \end{pmatrix} \quad (10)$$

$$\beta_n = \sqrt{(\mu_z/\mu_y)\beta^2 - k_0^2 \epsilon_x \mu_z} \quad (11)$$

Here d_p is the thickness of the p -th layer. We solved these eigenvalue equations and obtained the effective refractive index β_n/k_0 of each layer. With these results, we calculated the transmission characteristics of the metamaterial MMI using the Fourier expansion method, which is commonly used for MMI propagation analysis [34].

Figure 9 illustrates the example of the distribution profile of light traveling in the metamaterial MMI device. The intensity of the TE electric field at the cross-section (x - z plane) of the device is shown. The MMI is 15- μm wide, 650- μm long, and has a 450-nm-thick InP cladding layer. The wavelength of light is 1565 nm. Figure 9(a) shows our device with a 4-cut SRR array. The light traveling in the device suffers large propagation losses because of the magnetic interactions between the SRRs and light. Figure 9(b) shows the results for a control device with no-cut gold square rings having the same size as a 4-cut SRR. The no-cut ring has no resonant frequency and shows no magnetic interactions with 1.5- μm light; hence, the propagation loss is approximately 10 dB smaller than that of the 4-cut SRR. These results show that the 4-cut SRR array can successfully operate as a metamaterial layer at optical frequencies.

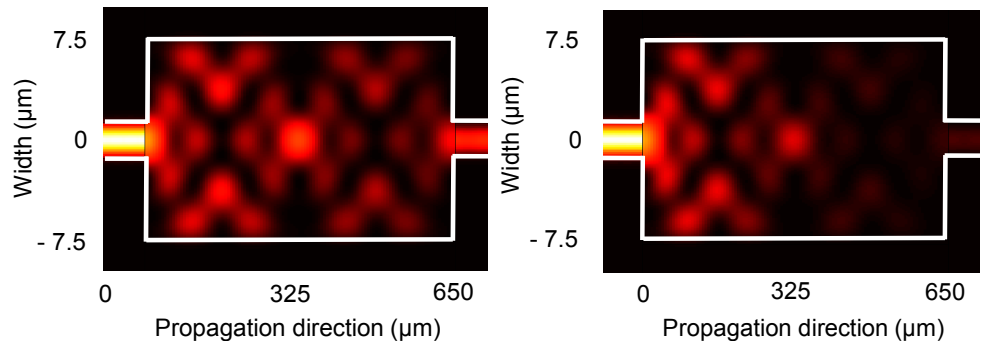


Fig. 9. Distribution profile of light traveling in metamaterial MMI device, calculated for devices with (a) 4-cut SRR array and (b) no-cut gold square rings. Electric field intensity at the cross-section (x - z plane) of the device is visualized by shading. Wavelength of light is 1565 nm.

3.3 Device fabrication and measurement

To move one step closer to the development of actual advanced optical-communication devices using the concept of metamaterials, we fabricated a trial device to confirm the magnetic response of a metamaterial comprising SRRs arrayed on a GaInAsP/InP 1×1 MMI coupler. The trial device was fabricated as follows. An undoped $\text{Ga}_{0.25}\text{In}_{0.75}\text{As}_{0.54}\text{P}_{0.46}$ core layer ($\lambda_g = 1.22 \mu\text{m}$, 200-nm thick) and an undoped InP cladding layer (420-nm thick) were grown on a (100) semi-insulating InP substrate by organometallic vapor phase epitaxy (OMVPE). On the surface of the cladding layer, SRRs consisting of Ti and Au layers were prepared using electron-beam lithography (EBL) and lift-off process.

The fabrication process is illustrated in Fig. 10 with both cross-sectional and plan views. The process flow was as follows: a resist layer of polymethyl methacrylate (PMMA) was first spin coated onto the InP cladding layer. Following spin coating, EBL was used to write a desired SRR array pattern onto the resist. The exposed areas of the resist were dissolved during development with xylene (Fig. 10(b)), resulting in a mask for the subsequent metal-evaporation process (Fig. 10(c)). Subsequently, the unexposed resist was removed along with the metal on top during lift-off with acetone (Fig. 10(d)). Figure 11 shows oblique scanning electron microscope (SEM) images of the SRR array fabricated according to this procedure. The SRRs were made of 5-nm-thick titanium and 20-nm-thick gold, and the dimensions of the individual SRR were designed on the basis of the simulation results shown in Section 3.2. In addition to experimental samples with 4-cut SRRs (Fig. 11(a)), we also made control samples with SRRs consisting of 2-cut Au/Ti square rings (Fig. 11(b)) with the same side length as that of the 4-cut SRR. This 2-cut SRR has a resonant frequency far lower than 193 THz, about 100 THz, so it does not interact with 1.5- μm light.

After the SRR array was formed, a 75-nm-thick SiO_2 film was deposited on the wafer by using plasma-enhanced chemical vapor deposition. Following the spin coating of PMMA, EBL was used again to write a 1×1 MMI pattern onto the resist (Fig. 10(e)). The width and length of the MMI were set to 15 μm and 660 μm . Finally, the exposed regions of the SiO_2 film and InP cladding layer were etched by using buffered HF and reactive ion etching (RIE), respectively, with a mixture gas of CH_4 and H_2 (Fig. 10(f)).

Figures 12(a) and 12(b) show the oblique and cross-sectional SEM images of the MMI region with 300×300-nm SRRs. In this study, the SiO_2 layer was not removed to prevent damages to the nanoscale SRR, which can be observed in Fig. 12(b). A thinner cladding layer (420 nm in Fig. 12(b)) is preferable to obtain large magnetic interactions even though it increases the propagation loss because the optical field coupled to the SRR metal is larger. The light phase is shifted by the magnetic interaction, but this can be neglected compared to the effect of the abovementioned propagation loss. Figure 12(c) shows the magnified plan of the trial device observed using an optical microscope. We made SRRs with different sizes from 300×300 to 550×550 nm (inside size of the square SRR ring). Both the width and gap of the SRR metal region were set to 75 nm.

In the following optical measurements, we observe the magnetic interactions of the propagating light and SRRs in the device. As described in Section 2, if magnetic interactions occur between the SRRs and light, the effective permeability of the SRR array becomes non-unity, i.e., large positive or negative values. At the same time, the imaginary part of the permeability increases from 0 to a finite value, and this implies that light is absorbed in the

device. Since it is possible to know the occurrence of the interaction by measuring the propagation loss of light in the device, we primarily measured the transmission and absorption of light in the device.

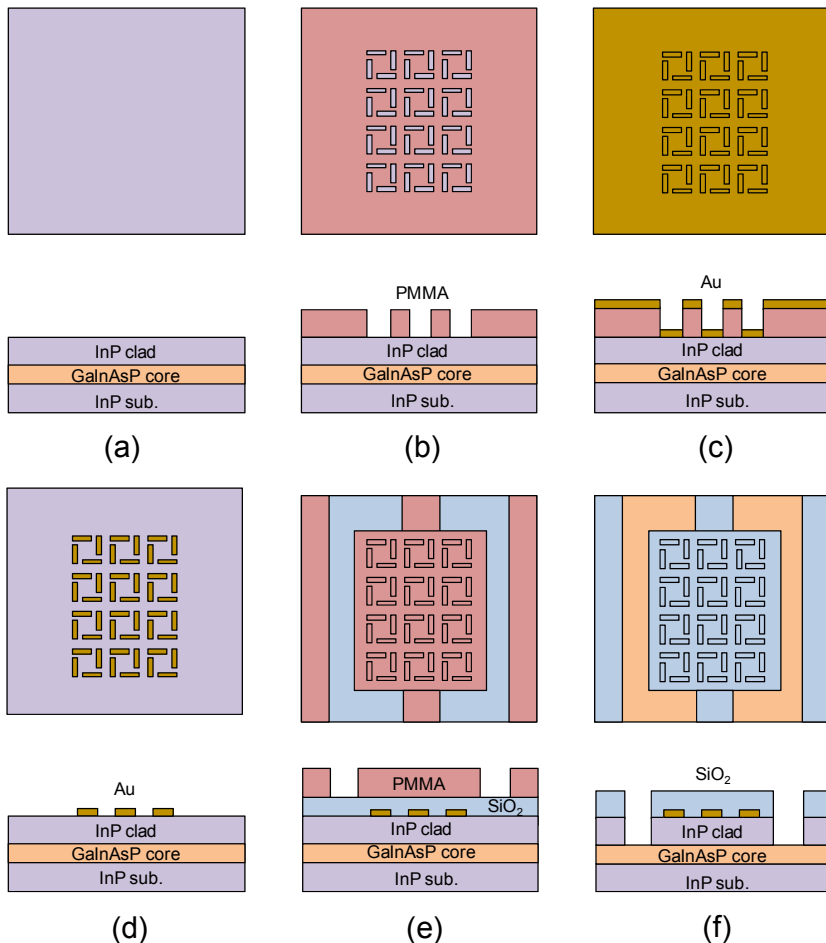


Fig. 10. Fabrication process for metamaterial MMI devices. SRR array was prepared using electron-beam lithography and lift-off process.

In the measurement, light was sent from a tunable laser to the device through a polarization controller. The wavelength was changed in a range of 1420-1575 nm. To clarify the effect of the magnetic interaction, we took the difference between the transmission intensity for the experimental samples (with 4-cut SRRs) and that for the control samples (with 2-cut SRRs). This difference shows an intrinsic change in transmission intensity induced by the SRR resonance without including parasitic factors such as wavelength-dependent ohmic loss in SRR metal, lensed-fiber coupling loss, and wavelength-dependent propagation characteristics in the MMI.

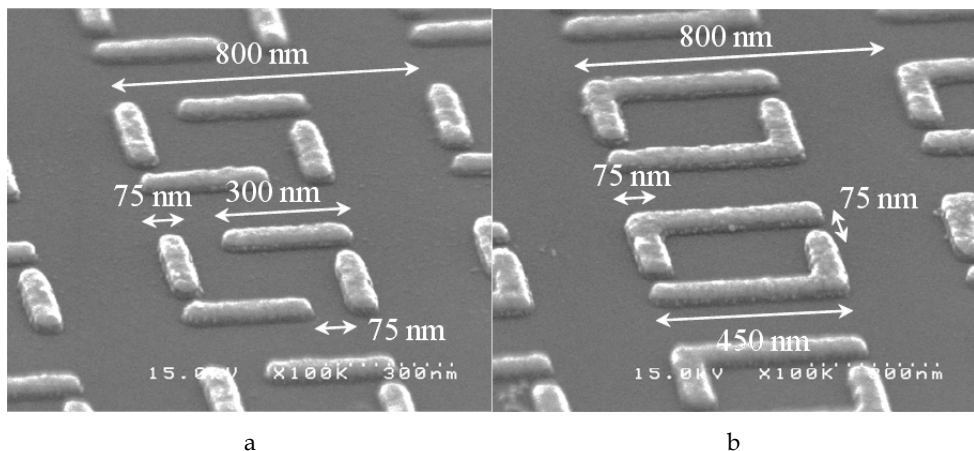


Fig. 11. (a) Enlarged oblique views of 4-cut SRRs, and (b) 2-cut SRRs observed with scanning electron microscopy.

Figure 13 plots the measured intensity difference for devices with a SRR size of (a) 300×300 nm 2 , (b) 350×350 nm 2 , (c) 400×400 nm 2 , and (d) 500×500 nm 2 as a function of wavelength. The magnetic interaction was observed clearly in the device with 350×350 -nm 2 SRRs (see Fig. 13(b)). That is, the intensity difference, induced by the SRR resonance, showed its peak at a wavelength of 1500 nm. The peak shifted to a shorter wavelength with smaller SRRs (Fig. 13(a)) and longer wavelength with larger SRRs (Fig. 13(c)), and both were out of this measurement range. With 500×500 -nm 2 SRRs, the intensity difference was almost 0 at this wavelength range (Fig. 13(d)), which showed that no SRR resonance occurred at 1.5- μ m wavelength. These wavelength-dependent and SRR-size-dependent transmission characteristics show that the magnetic field of light interacted successfully with the SRRs to produce magnetic resonance at optical frequency. In contrast, no intensity change was observed for the TM mode. This polarization-wavelength dependent absorption is positive proof that the magnetic interaction was successfully established in our device for the TE-mode light. In this manner, we can realize *non-unity* permeability in InP-based photonic devices by using the SRR metamaterial

Furthermore, for the TE mode, a magnetic field perpendicular to the axis of the split-ring, by virtue of Ampere's law, created a circulating current via the charge accumulation at the gap (see Section 2 for details). Due to the presence of gaps, the resulting charge distribution was asymmetric; this results in charge accumulation around the capacitive gaps and induces an electric dipole moment. On the other hand, for the TM mode, an electric field is present parallel to the two symmetric sides of the split-ring, whereas in the approximation of the thin metallization, the current in the perpendicular directions was negligible. In addition, the size of the ring was smaller than the incident wavelength, and this ensured that the variations in the electric field between the two sides were also negligible for a first approximation. Consequently, the charge distribution resulting from this incidence was symmetric and did not generate a circulating current.

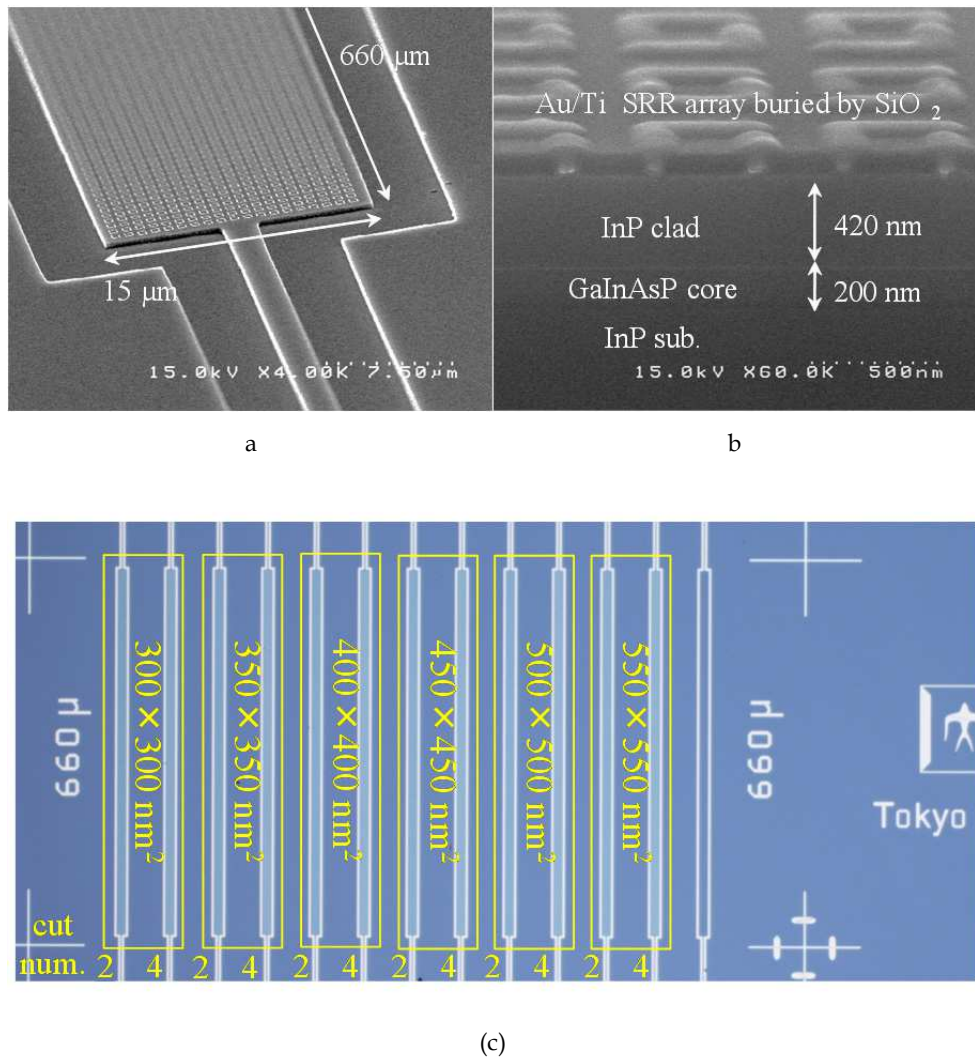


Fig. 12. (a) Oblique views of completed device and (b) cross-sectional view of 300×300-nm SRRs buried in SiO_2 layer; (c) Plan view of GaInAsP/InP 1×1 MMI coupler with SRR array observed with optical microscopy.

The equivalent permeability and permittivity of the SRR array layer are a function of wavelength. To know their values exactly, we must know both intrinsic absorption loss and phase shift of propagating light in the device. However, we cannot extract each separately from the transmission data shown in Fig. 13. So then, to cope with the problem, we have recently proposed a measurement method that uses a Mach-Zehnder interferometer (MZI) and successfully retrieved constitutive parameters for the SRR array. The following Section provides the outline of the results.

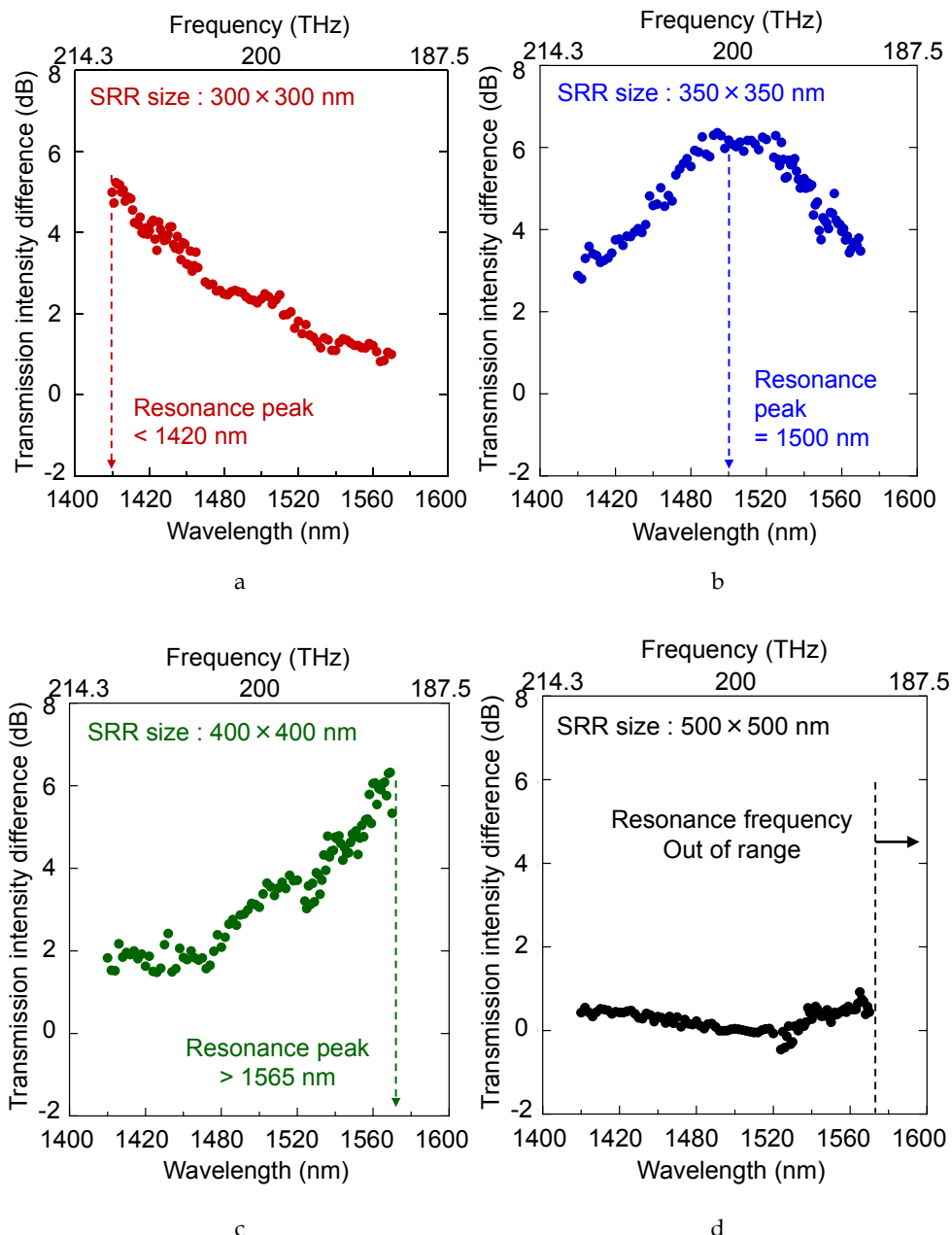


Fig. 13. (Color online) Transmission-intensity difference (or transmission spectra) for devices with SRR size of (a) $300 \times 300 \text{ nm}^2$, (b) $350 \times 350 \text{ nm}^2$, (c) $400 \times 400 \text{ nm}^2$, and (d) $500 \times 500 \text{ nm}^2$ as a function of wavelength from 1420 to 1575 nm, measured for TE-mode light.

4. Permeability retrieval in III-V semiconductor-based waveguide device with metamaterials

The accurate permeability values in waveguide-based photonic devices is a very important factor, since it mostly determines their performance. Accurate permeability data, however, cannot be extracted from the simple transmission data of the previous devices because the transmission data also includes both the effect of SRR's effective permittivity and permeability. In this Section, we have proposed a measurement method that uses a Mach-Zehnder interferometer (MZI) and successfully retrieved constitutive parameters for the SRR array.

Our MZI device is shown in Fig. 14(d). It consists of two 3-dB couplers and two arms made with GaInAsP/InP ridge waveguides, with a metal SRR array attached on one of the arms. For TE-mode input light with the SRR-resonance frequency, the SRR array interacts with the light, thereby behaving as a material with a complex refractive-index. The real part of the refractive-index mainly affects the phase of traveling light, thereby changing the phase difference at the output coupler. The imaginary part mainly causes the propagation loss of light in the arm. Therefore, the transmittance of the MZI is determined by the phase difference and propagation loss.

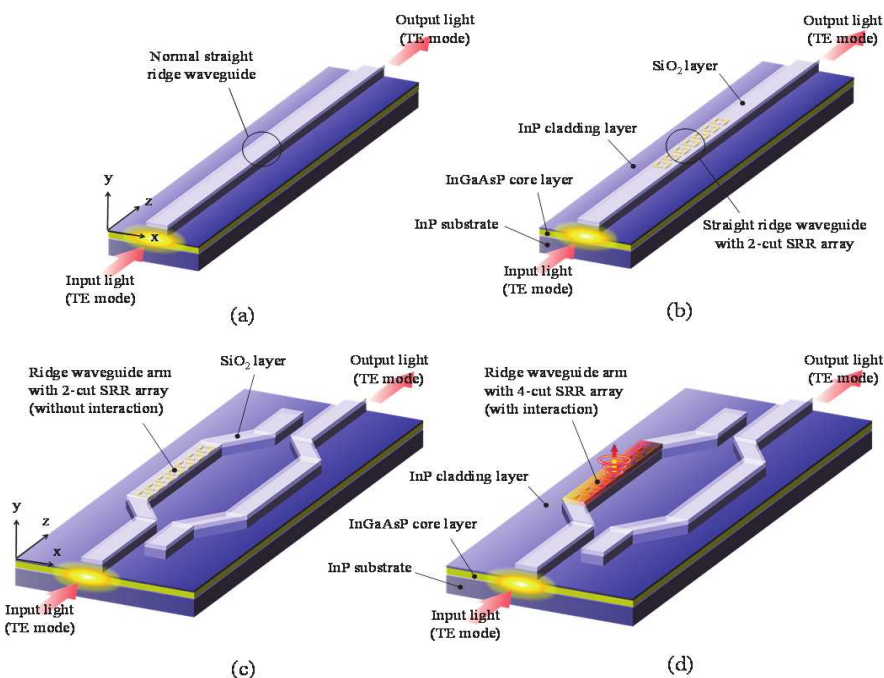


Fig. 14. GaInAsP/InP straight ridge waveguide without SRRs (a) and with 2-cut SRRs (b); Mach-Zehnder Interferometer consisting of GaInAsP/InP waveguides and (c) 2-cut / (d) 4-cut SRR array attached on one arm.

The propagation loss in the arms can be inferred from the transmission data of straight waveguides with/without the SRR array shown in Figs. 14(a) and 14(b). Therefore, the effective permeability and permittivity of the SRR array can be calculated, using measured data for the transmittance of the MZI.

An actual MZI was made for measurement at 1.5- μm optical communication wavelength. Epitaxial layer structures were the same as those of our previous device. On the surface of the device, an SRR array (consisting of 10-nm thick Ti and 40-nm thick Au) was formed using electron-beam lithography (EBL) and a lift-off process. Figure 15(a) shows the oblique images of the SRR array observed with a scanning electron microscope (SEM). The 4-cut SRR was used because it has a high resonant frequency owing to its small gap capacitance as stated in Section 2.

The size of the SRR was designed for use at 1.5- μm band frequency (193 THz). After the formation of the SRR array, a SiO₂ mask (100-nm thick) for the MZI pattern was formed on the device with plasma-enhanced chemical-vapor-deposition and EBL. With the SiO₂ mask, the MZI structure was formed using CH₄/H₂ reactive ion etching. Figure 15(b) shows the SEM image of the arms with/without the SRR array. The length of the SRR array along the arm was set to 500 μm . In addition to these experimental samples, straight ridge waveguides with/without the SRRs were made. We also prepared control samples with SRRs consisting of 2-cut square rings with the same size as that of the 4-cut SRR. As mentioned in Section 3, the 2-cut SRR has a resonant frequency far higher than 193 THz, so it has no interaction with 1.5- μm light.

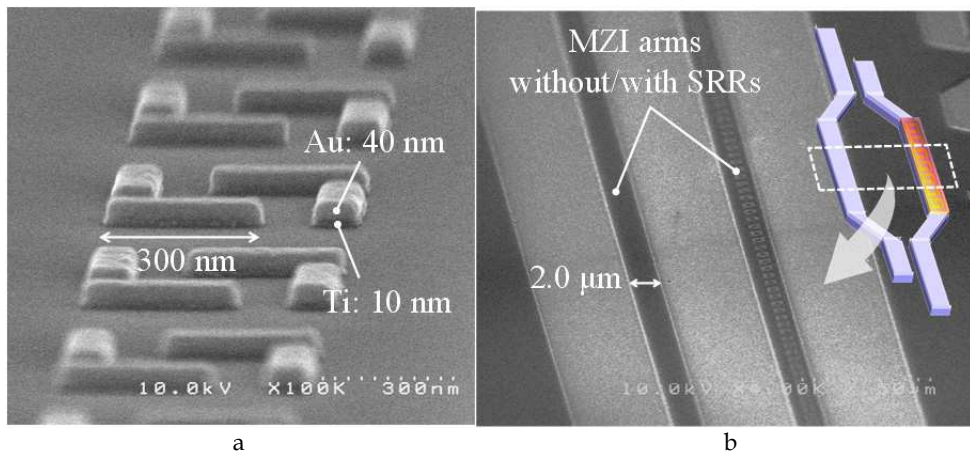


Fig. 15. SRRs and arms of MZI: (a) oblique view of 4-cut SRRs, and (b) two arms, observed with scanning electron microscopy.

Figure 16(a) shows the output intensity for straight waveguides with 4-cut SRR array (blue dots), without SRRs (black dots), and with 2-cut SRRs (red dots). The difference between the curves without SRRs and that with 2-cut SRRs corresponds to a loss caused by light absorption of the SRR metal. The difference between the 2-cut SRRs and 4-cut SRRs shows the loss caused by the magnetic interaction between the SRRs and light. The 4-cut SRRs resonated at about 1510-1520 nm and showed the maximum loss at this wavelength.

Figure 16(b) shows the output intensity for MZIs with 4-cut SRRs and that for without SRRs. Their difference shows the intensity change induced by the phase shift and the absorption loss of light in the MZI. That is, the difference shows an intrinsic change in transmission intensity induced by the SRR resonance without including parasitic factors such as metal absorption loss in the SRRs and lensed-fiber coupling loss in the measurement system.

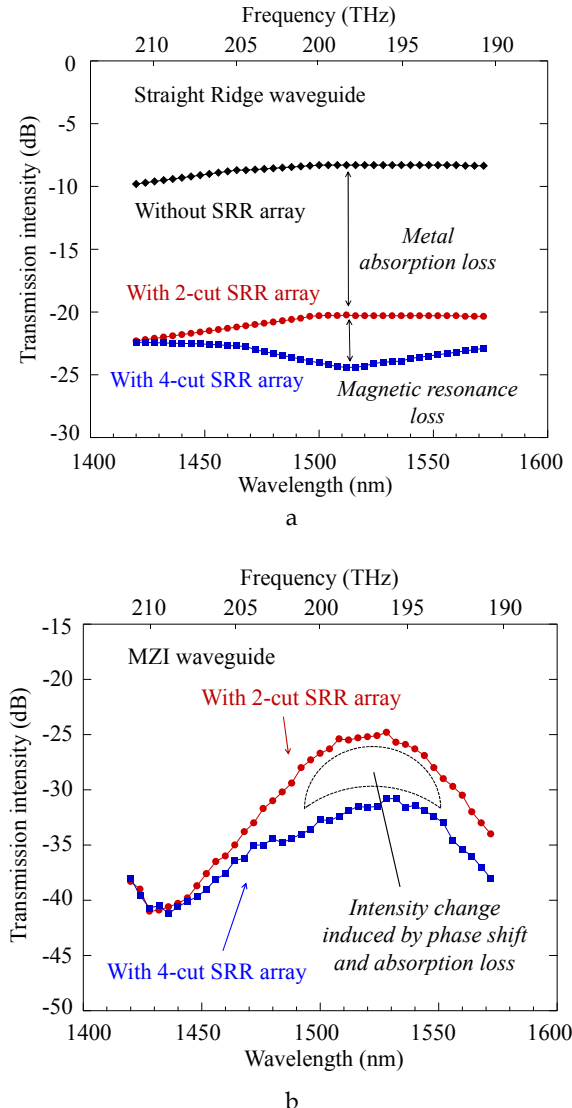


Fig. 16. Output intensity from devices with 4-cut SRRs (blue lines), 2-cut SRRs (red lines) and without SRRs (black lines) as a function of wavelength, measured for (a) straight ridge waveguides and (b) MZIs.

On simple condition that the electric and magnetic fields are constant in the x-direction, that is, $\partial_x = 0$, the wave equation in each layer of the device is given by Eq. (7) in Section 2.

$$\partial_y^2 E_x + \left(k_0^2 \epsilon_x \mu_z - \frac{\mu_z}{\mu_y} \beta^2 \right) E_x = 0 \quad (12)$$

To extract the permittivity ϵ_x of the SRR array without resonance, we used the difference between the transmission intensity of the straight waveguides with 2-cut SRRs and that of the control device without SRRs. The permittivity ϵ_x of the SRR array can be calculated, using the transfer-matrix method with Eq. (12) (μ_y and μ_z in Eq. (12) are equal to 1 because the SRRs have no resonance). After that, the real and imaginary parts of permeability μ_y of the SRR array was retrieved, using the obtained permittivity ϵ_x and the transmission intensity ratio (= (2-cut SRRs)/(4-cut SRRs)) for the straight waveguide and that for the MZI. In calculation, the effective thickness of the SRR layer was set to 350 nm.

Figure 17 shows the retrieved permeability (real and imaginary parts) of the SRR array as a function of frequency. The permeability exhibited a resonance at 200 THz, and the real part of the relative permeability changed from +2.2 to -0.3 in the vicinity of this frequency. This results show the feasibility of semiconductor-based photonic devices combined with metamaterials.

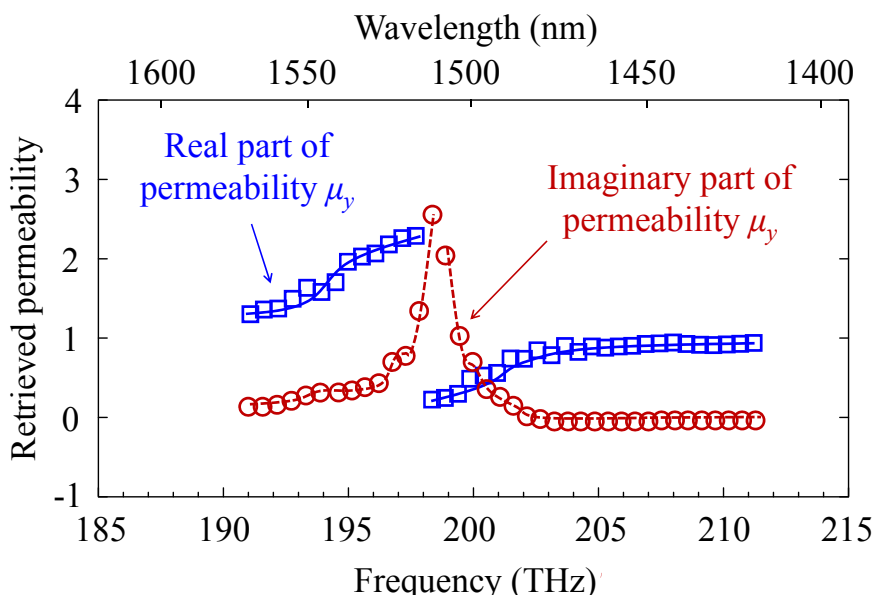


Fig. 17. Retrieved effective permeability (real and imaginary parts) of SRR array on MZI waveguide, plotted as a function of frequency.

5. Conclusion

Realizing *non-unity* permeability at optical frequencies can be expected to lead us to advanced optical-communication devices based on novel operation principles. To move one step closer to this goal, in this paper, we have demonstrated that the permeability in semiconductor photonic devices can be controlled using the concept of metamaterials.

As an actual example, we fabricated a GaInAsP/InP MMI device combined with an SRR array that operated as a metamaterial layer. The operation wavelength was set as 1.55 μm . The transmission characteristics of this metamaterial MMI device strongly depended on the polarization and wavelength of input light. This shows that the SRR array layer interacted with the magnetic field of light and produced magnetic resonance at optical frequencies. After that, to know constitutive parameters in the device exactly, we have proposed a measurement method that uses a MZI and successfully retrieved the accurate permeability value for the SRR array. The permeability exhibited a resonance at 200 THz, and the real part of the relative permeability changed from +2.2 to -0.3 in the vicinity of this frequency. Our results show the feasibility of III-V semiconductor-based waveguide photonic devices combined with metamaterials. This would be useful in the development of novel optical-communication devices.

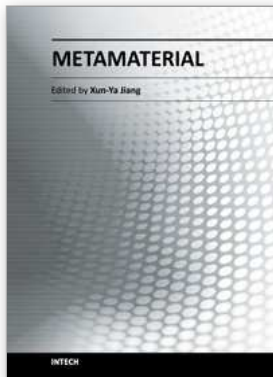
6. References

- [1] R. M. Walser, "Electromagnetic metamaterials," in *Proc. SPIE*, vol. 4467, pp. 1-15 (2001).
- [2] H. J. Lezec, J. A. Dionne, and H. A. Atwater, "Negative refraction at visible frequencies," *Science*, vol. 316, no. 5823, pp. 430-432 (2007).
- [3] W. Cai, U. K. Chettiar, H. K. Yuan, V. C. de Silva, A. V. Kildishev, V. P. Drachev, and V. M. Shalaev, "Metamagnetics with rainbow colors," *Optics Express*, vol. 15, no. 6, pp. 3333-3341 (2007).
- [4] J. Valentine, S. Zhang, T. Zentgraf, E. Ulin-Avila1, D. A. Genov1, G. Bartal1, and X. Zhang, "Three-dimensional optical metamaterial with a negative refractive index," *Nature*, vol. 455, no. 7211, pp. 376-379 (2008).
- [5] D. Schurig, J. J. Mock, B. J. Justice, S. A. Cummer, J. B. Pendry, A. F. Starr, and D. R. Smith, "Metamaterial electromagnetic cloak at microwave frequencies," *Science*, vol. 314, no. 5801, pp. 977-980 (2006).
- [6] J. B. Pendry, "Negative refraction makes a perfect lens," *Phys. Rev. Lett.*, vol. 85, no. 18, pp. 3966-3969 (2000).
- [7] R. Nagarajan, C. H. Joyner, R. P. Schneider, Jr., J. S. Bostak, T. Butrie, A. G. Dentai, V. G. Dominic, P. W. Evans, M. Kato, M. Kauffman, D. J. H. Lambert, S. K. Mathis, A. Mathur, R. H. Miles, M. L. Mitchell, M. J. Missey, S. Murthy, A. C. Nilsson, F. H. Peters, S. C. Pennypacker, J. L. Pleumeekers, R. A. Salvatore, R. K. Schlenker, R. B. Taylor, H. S. Tsai, M. F. Van Leeuwen, J. Webjorn, M. Ziari, D. Perkins, J. Singh, S. G. Grubb, M. S. Reffle, D. G. Mehuyts, F. A. Kish, and D. F. Welch, "Large-scale photonic integrated circuits," *IEEE J. Select. Topics Quantum Electron.*, vol. 11, no. 1, pp. 50-65, (2005).

- [8] J. Van Campenhout, P. R. Romeo, P. Regreny, C. Seassal, D. Van Thourhout, S. Verstuyft, L. D. Cioccio, J.-M. Fedeli, C. Lagahe, R. Baets, "Electrically pumped InP-based microdisk lasers integrated with a nanophotonic silicon-on-insulator waveguide circuit", *Optics Express*, vol. 15, no. 11, pp. 6744-6749 (2007).
- [9] M. J.R. Heck, P. Muñoz, B. W. Tilma, E. A.J.M. Bente, Y. Barbarin, Y. S. Oei, R. Nötzel and M. K. Smit, "Design, Fabrication and Characterization of an InP-based Tunable Integrated Optical Pulse Shaper", *IEEE Journal of Quantum Electron.*, vol. 44, no. 4, p.p. 370-377 (2008).
- [10] S. C. Nicholes, M. L. Masanović, B. Jevremović, E. Lively, L. A. Coldren, and D. J. Blumenthal, "World's first InP 8x8 monolithic tunable optical router (MOTOR) operating at 40 Gbps line rate per port," in *Proc. Optical Fiber and Communication Conference*, PDPB1 (2009).
- [11] C. R. Doerr, L. Zhang, and P. J. Winzer, "Monolithic InP multi-wavelength coherent receiver," in *Proc. Optical Fiber and Communication Conference*, PDPB1 (2010).
- [12] J. J. G. M. van der Tol, Y. S. Oei, U. Khalique, R. Nötzel, and M. K. Smit, "InP-based photonic circuits: Comparison of monolithic integration techniques (review paper)," *Prog. Quantum Electron.*, vol. 34, no. 4, pp. 135-172 (2010).
- [13] I. V. Shadrivov, A. A. Sukhorukov, Y. S. Kivshar, "Guided modes in negative-refractive-index waveguides," *Phys. Rev. E*, vol. 67, no. 5, 057602 (2003).
- [14] A. C. Peacock and N. G. R. Broaderick, "Guided mode in channel waveguide with a negative index of refraction," *Optics Express*, vol. 11, no. 20, pp. 2502-2510 (2003).
- [15] K. L. Tsakmakidis, A. D. Boardman, and O. Hess, "Trapped rainbow storage of light in metamaterials," *Nature*, vol. 450, no. 7168, pp. 397-401 (2007).
- [16] A. Figotin and I. Vitebskiy, "Slow-wave resonance in periodic stacks of anisotropic layers," *Phys. Rev. A*, vol. 76, no. 5, 053839 (2007).
- [17] K.-Y. Jung, F. L. Teixeira, and R. M. Reano, "Au/SiO₂ nanoring plasmon waveguides at optical communication band," *IEEE Journal of Lightwave Technology*, vol. 25, no. 9, pp. 2757-2765 (2007).
- [18] K.-Y. Jung and F. L. Teixeira, "Photonic crystals with a degenerate band edge: Field enhancement effects and sensitivity analysis," *Phys. Rev. B*, vol. 77, no. 12, 125108 (2008).
- [19] G. Adamo, K. F. MacDonald, F. De Angelis, E. Di Fabrizio, and N. I. Zheludev, "Nanoscale electron-beam-driven metamaterial light sources," in *Proc. 23rd Annual Meeting of the IEEE Photonics Society*, WM2 (2010).
- [20] K. Dani, Z. Ku, P. C. Upadhyaya, R. P. Prasankumar, S. R. Brueck, and A. J. Taylor, "Subpicosecond optical switching with a negative index metamaterial," *Nano Lett.*, vol. 9, no. 10, 3565-3569 (2009).
- [21] D. J. Cho, W. Wu, E. Ponizovskaya, P. Chaturvedi, A. M. Bratkovsky, S. Y. Wang, X. Zhang, F. Wang, and Y. R. Shen, "Ultrafast modulation of optical metamaterials," *Opt. Express*, vol. 17, no. 20, 17652-17657 (2009).
- [22] Keshav M. Dani, Zahyun Ku, Prashanth C. Upadhyaya, Rohit P. Prasankumar, Antoinette J. Taylor, and S. R. J. Brueck, "Ultrafast modulation of optical metamaterials," *Opt. Express*, vol. 19, no. 5, 3973-3983 (2011).

- [23] T. Amemiya, T. Shindo, D. Takahashi, N. Nishiyama, S. Arai, "Magnetic Interactions at Optical Frequencies in an InP-Based Waveguide Device with Metamaterial," *IEEE J. Quantum Electronics*, Vol. 47, No. 5, pp. 736-744 (2011).
- [24] T. Amemiya, T. Shindo, D. Takahashi, S. Myoga, N. Nishiyama, S. Arai, "Nonunity permeability in metamaterial-based GaInAsP/InP multimode interferometers," *Optics Lett.*, Vol. 36, No. 12, pp. 2327-2329, Jun. 2011.
- [25] H. T. Chen, *et al.*, "Active terahertz metamaterial devices," *Nature*, vol. 444, no. 7119, pp. 597-600 (2006).
- [26] T. Driscoll, *et al.*, "Memory Metamaterials," *Science* vol. 325, no. 5947, pp. 1518-1521 (2009).
- [27] S. Zhang, W. Fan, N. C. Panoiu, K. J. Malloy, R. M. Osgood, and S. R. J. Brueck, "Experimental demonstration of near-infrared negative-index metamaterials," *Phys. Rev. Lett.* vol. 95, no. 13, 137404 (2005).
- [28] Z. Ku, and S. R. J. Brueck, "Comparison of negative refractive index materials with circular, elliptical and rectangular holes," *Opt. Express* vol. 15, no. 8, 4515-4522 (2007).
- [29] T. J. Yen, W. J. Padilla, N. Fang, D. C. Vier, D. R. Smith, J. B. Pendry, D. N. Basov, and X. Zhang, "Terahertz magnetic response from artificial materials," *Science*, vol. 303, no. 5663, pp. 1494-1496 (2004).
- [30] S. Zhang, W. Fan, B. K. Minhas, A. Frauenglass, K. J. Malloy, and S. R. J. Brueck, "Midinfrared resonant magnetic nanostructures exhibiting a negative permeability," *Phys. Rev. Lett.*, vol. 94, no. 3, 037402 (2005).
- [31] C. Enkrich, M. Wegener, S. Linden, S. Burger, L. Zschiedrich, F. Schmidt, J. F. Zhou, Th. Koschny, and C. M. Soukoulis, "Magnetic metamaterials at telecommunication and visible frequencies," *Phys. Rev. Lett.*, vol. 95, no. 20, 203901 (2005).
- [32] S. Linden, C. Enkrich, G. Dolling, M. W. Klein, J. Zhou, T. Koschny, C. M. Soukoulis, S. Burger, F. Schmidt, and M. Wegener, "Photonic metamaterials: magnetism at optical frequencies," *IEEE J. Select. Topics Quantum Electron.*, vol. 12, no. 6, pp. 1097-1105 (2006).
- [33] C. E. Kriegler, M. S. Rill, S. Linden, and M. Wegener, "Bianisotropic photonic metamaterials," *IEEE J. Select. Topics Quantum Electron.*, vol. 16, no. 2, pp. 367-375 (2010).
- [34] S. Ramo, J. R. Whinnery, and T. V. Duzer., *Field and Waves in Communication Electronics* (Wiley 1993), pp. 149-156.
- [35] A. Ishikawa, T. Tanaka, and S. Kawata, "Frequency dependence of the magnetic response of split-ring resonators," *J. Opt. Soc. Am. B*, vol. 24, no. 3, pp. 510-515 (2007).
- [36] S. A. Ramakrishna, "Physics of negative refractive index materials," *Rep. Prog. Phys.*, vol. 68, no. 2, pp. 449-521 (2005).
- [37] A. Ishikawa, T. Tanaka, and S. Kawata, "Negative magnetic permeability in the visible light region," *Phys. Rev. Lett.*, vol. 95, no. 23, 237401 (2005).
- [38] D. R. Smith and J. B. Pendry, "Homogenization of metamaterials by field averaging (invited paper)," *J. Opt. Soc. Am B*, vol. 23, no. 3, pp. 391-403 (2006).

- [39] L. B. Soldano and E. C. M. Pennings, "Optical multi-mode interference devices based on self-imaging: principles and applications," *IEEE J. Lightwave Technol.*, vol. 13, no. 4, pp. 615–627 (1995).



Metamaterial

Edited by Dr. Xun-Ya Jiang

ISBN 978-953-51-0591-6

Hard cover, 620 pages

Publisher InTech

Published online 16, May, 2012

Published in print edition May, 2012

In-depth analysis of the theory, properties and description of the most potential technological applications of metamaterials for the realization of novel devices such as subwavelength lenses, invisibility cloaks, dipole and reflector antennas, high frequency telecommunications, new designs of bandpass filters, absorbers and concentrators of EM waves etc. In order to create a new devices it is necessary to know the main electrodynamical characteristics of metamaterial structures on the basis of which the device is supposed to be created. The electromagnetic wave scattering surfaces built with metamaterials are primarily based on the ability of metamaterials to control the surrounded electromagnetic fields by varying their permeability and permittivity characteristics. The book covers some solutions for microwave wavelength scales as well as exploitation of nanoscale EM wavelength such as visible specter using recent advances of nanotechnology, for instance in the field of nanowires, nanopolymers, carbon nanotubes and graphene. Metamaterial is suitable for scholars from extremely large scientific domain and therefore given to engineers, scientists, graduates and other interested professionals from photonics to nanoscience and from material science to antenna engineering as a comprehensive reference on this artificial materials of tomorrow.

How to reference

In order to correctly reference this scholarly work, feel free to copy and paste the following:

T. Amemiya, T. Shindo, S. Myoga, E. Murai, N. Nishiyama and S. Arai (2012). Non-Unity Permeability in InP-Based Photonic Device Combined with Metamaterial, Metamaterial, Dr. Xun-Ya Jiang (Ed.), ISBN: 978-953-51-0591-6, InTech, Available from: <http://www.intechopen.com/books/metamaterial/non-unity-permeability-in-inp-based-photonic-device-combined-with-metamaterial>



InTech Europe

University Campus STeP Ri
Slavka Krautzeka 83/A
51000 Rijeka, Croatia
Phone: +385 (51) 770 447
Fax: +385 (51) 686 166
www.intechopen.com

InTech China

Unit 405, Office Block, Hotel Equatorial Shanghai
No.65, Yan An Road (West), Shanghai, 200040, China
中国上海市延安西路65号上海国际贵都大饭店办公楼405单元
Phone: +86-21-62489820
Fax: +86-21-62489821

© 2012 The Author(s). Licensee IntechOpen. This is an open access article distributed under the terms of the [Creative Commons Attribution 3.0 License](#), which permits unrestricted use, distribution, and reproduction in any medium, provided the original work is properly cited.